Hindawi
International Journal of RF and Microwave Computer-Aided Engineering
Volume 2024, Article ID 8948916, 20 pages
https://doi.org/10.1155/2024/8948916

Research Article

Analysis and Design of a High Gain Multiband Antenna Based on Metamaterials for RFID Applications

Mahdi Abdelkarim, Ali Gharsallah, and Rihab Faouel

Laboratory for Research on Microwave Electronics, Physics Department, Faculty of Sciences, University of Tunis El Manar, Tunis, Tunisia

Correspondence should be addressed to Mahdi Abdelkarim; mahdi.abdelkarim@gmail.com

Received 10 October 2023; Revised 9 February 2024; Accepted 13 February 2024; Published 5 March 2024

Academic Editor: Wen-Jun Lu

In this research work, the design of a dipole antenna based on metamaterials is proposed, which can be used as a high gain multiband communication device for RFID applications. This antenna is printed on two sides of an Arlon substrate, which has an overall electrical dimension of $0.39\,\lambda_0 \times 0.11\,\lambda_0 \times 0.0014\,\lambda_0$. The metamaterials are used to obtain a multiband antenna, and their integration technique into the antenna results in a high gain compared to a conventional antenna without any magnification or additional layer. The simulated and measured results show that the proposed antenna can operate at 0.88-0.97 GHz, 2.41-2.48 GHz, and 5.77-5.91 GHz with a reflection coefficient of less than −10 dB, which make it well suited for RFID at 860-960 MHz and 2.4 GHz/5.8 GHz. All these resonant frequencies show better impedance matching with high gain. The proposed antenna has the advantages of simple design, low profile, easy feeding, low manufacturing cost, and easy integration into the electronic circuit.

1. Introduction

In recent decades, the rapid development and expansion of advanced wireless technologies such as RFID, GPS, GSM, Bluetooth, WLAN, WiMAX, and 5G NR has led to new requirements for small communication devices that can perform various functions and provide multiple services. In these wireless applications, it is becoming increasingly difficult to integrate multiple antennas into a single device, because having more than one antenna to cover multiple frequencies makes the terminal quite large and leads to mutual coupling when each frequency band is generated by a single antenna. This method not only leaves space for additional components and lowers costs to increase customer interest but also improves communications in operation by reducing weight and avoiding complexity and losses in the coverage network. This challenging task has led antenna designers to look for a multifunctional antenna that can, in particular, cover several frequency bands at the same time, such as RFID at UHF (860-960 MHz) and SHF (2.4/5.8 GHz) without interference with coexisting bands. In addition, a multifunctional antenna with low manufacturing cost, easy feeding, light weight, and easy integration into an environment with microwave components is one of the most important requirements in RFID application. However, operating an antenna in multiple bands without inevitable performance degradation is still an important area. This is because the antenna performance, which directly determines the quality of the communication system, rarely remains unchanged with the demand for multiband capabilities. Therefore, various approaches and techniques have been proposed to develop multiband features in a single structure and maintain or improve its performance. These techniques include slots, parasitic elements, differential feeding, frequency selective surfaces (FSS), metamaterials, and stacked patches. Indeed, slots have attracted much attention. In ref [1], a three-band antenna with circular slot technology is proposed for WLAN/WiMAX communication. By using this

technique, the antenna has achieved significant impedance matching at all three resonant frequencies. However, it is difficult to achieve the high gain.

In ref [2], a ring-shaped dual-band slot antenna with an integrated filtering network is used to miniaturize the antenna size. Since the size of the antenna is influenced by the slot, the gain/efficiency effect should be considered when designing the antenna. The antenna in ref [3], with an overall size of $100 \times 160 \times 1.6\,\text{mm}^3$, achieves a dual-band UHF 0.915/2.45 GHz RFID reader by bending a metallic conductor spiral with five turns. By combining these elements, the radiation pattern can be set low, especially at 2.45 GHz, although this antenna is very large and does not cover the SHF band. L-shaped slots [4] and star-shaped fractal slots [5] are integrated on the radiating patch to increase the number of frequency bands and improve the gain to cover wireless systems. By inserting these slots, the effective length of the antenna is increased, resulting in better impedance matching and consequently a reduction in size. However, this can lead to a deterioration in the performance of the antenna in terms of gain and directivity. Another technique [6–10] has been proposed to obtain a multiband antenna with smaller size, namely, to change the shape of the antenna, which can drastically reduce the amplitude of the current distribution in the radiator near the ground to suppress unbalanced current. Although these antennas have the advantage of compact size, the gain of the antennas remains very low. This trade-off relationship between antenna performance and size can be reduced by using multilayer substrates made of different materials. In [11], a three-port triband antenna with slot-coupled feed technique on three-layer substrates for radio frequency identification (RFID) is presented. Similarly, multiband patch antennas with feed technique implemented on two-layer substrates [12–14] and three-layer substrates [15] are proposed for wireless applications. An increase in bandwidth could be achieved together with a gain. In addition, these antennas can be used to generate circularly polarized radiation. However, due to the multilayer substrate and the multiple feed technique, the fabrication of this type of structure is complicated and very large. In addition, multiple feeding techniques and extra space are usually required to develop and place the multilayer substrates. To overcome this problem, several research papers have proposed a technique that combines two structures of the same shape and different sizes, with each radiating element supporting one or the other operating band. The antennas in refs [16–20] achieve two-band coverage by combining moxon and quasi-Yagi, stacked patches, dipoles, four dipoles, or patch and dipole array. These structures are simple, can be easily integrated into other RF microwave circuits, and provide better gain than conventional antenna radiators because antenna's radiated power can be increased by changing the radiating structure. However, only a dual band can be achieved that can cover only one wireless application, so an extra space is needed to add a new radiating element. This technique could be improved by combining the parasitic elements [21–23] with a modified antenna. Although these structures are useful for WLAN/WiMAX with a simple and compact size, they do not cover the UHF RFID band. For all these reasons, several works have addressed the use of metamaterials (MTM) to enhance the performance of the antenna and achieve multiband capability, as metamaterials produce more additional resonant modes when the input impedance of the antenna is changed. By loading metamaterial elements [24–27] with a radiating patch, different resonant modes can be achieved near the main frequency served by the radiating patch because coupling has occurred between the radiating patch and these elements. For all these structures, the maximum achievable gain is of the order of 2-6 dB in the UHF and SHF bands, which is not suitable for RFID application because the antenna, which has low performance in terms of gain and directivity, may cause tag detection errors or losses in the supply network in other applications, thus limiting the range of applications. There are numerous techniques based on metamaterials that can be employed above [28], or inside the radiating element [29–31]. However, only a single band has been successfully achieved around 2.4 GHz, with a maximum gain of 6 dB, at the expense of increased size. The problem is that there is a trade-off between space and performance constraints. To overcome this problem, this paper investigates the design of a dipole antenna based on metamaterials that can perform multiple functions effectively and simultaneously, with the aim of achieving multiband characteristics along with high gain. This antenna is not only suitable for multiband RFID application but also provides low manufacturing cost, easy feeding, light weight, and easy integration into an environment with microwave components. After the introduction, this article is divided into 6 sections as mentioned below. Section 2 presents the design of the dipole antenna with its equivalent circuit. In Section 3, the split-ring resonator (SRR) with its equivalent circuit is studied. Then, the antenna design methodology using metamaterials is analyzed and studied with a parametric study to shed light on the effects of different parameters on the antenna performance. In Section 4, an analysis of the proposed antenna is performed in terms of return loss, current distribution, gain, and pattern. Finally, a comparison is made between the proposed antenna and the state of the art.

2. Dipole Antenna Configuration

Following previous studies in the literature [32–34], two symmetrical arms with dimensions $W_1 \times W_d$ are printed on the top and bottom of the substrate to obtain a dipole antenna. This antenna is constructed on a 0.49 mm thick Arlon CuClad 250LX substrate with a relative permittivity of 2.42 and a loss tangent of 0.0018 and fed directly via a microstrip line to achieve a matching impedance of 50 Ω. Figure 1 shows the upper and lower view of the dipole antenna design. The original dipole antenna with overall dimensions of $131.6 \times 34 \times 0.49\,\text{mm}^3$ (equivalent to $0.39\,\lambda_0 \times 0.11\,\lambda_0 \times 0.0014\,\lambda_0$) is designed to be centered at 1 GHz, and the harmonic frequency, defined as f_1, is 2 GHz. All design parameters are listed in Table 1.

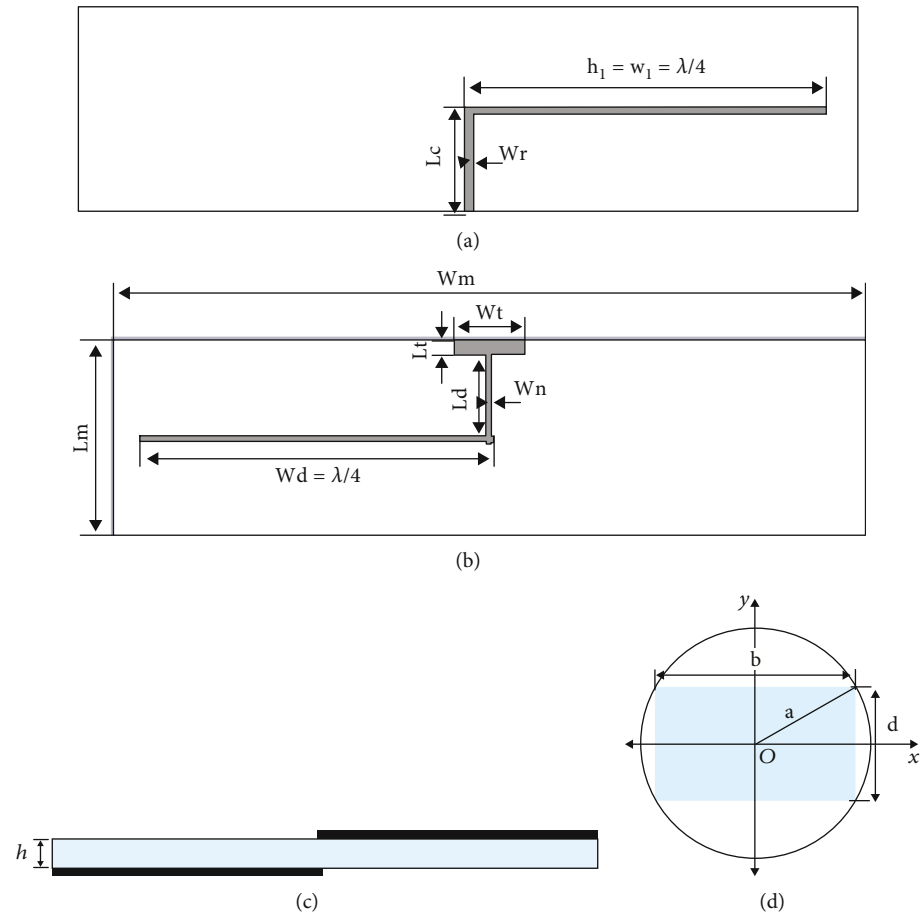

Figure 1: Design of dipole antenna: (a) top view, (b) bottom view, (c) side view, and (d) radius of the rectangle.

The dipole antenna can be modelled by its equivalent circuit diagram, as shown in Figure 2(a) [35]. The circuit consists of inductive and capacitive load elements, whereby the two arms of the antenna are replaced by a series combination of capacitance and inductance and a parallel combination of resistance, capacitance, and inductance.

Define W_{01} as the first resonant frequency and W_{02} as the second resonant frequency at which the antenna's reactance vanishes. R_0 is the resistance at W_{01}, and R_1 is the resistance at W_{02}.

C_0 represents the antenna capacitance at a frequency f that is well below the first resonance, as specified in the following equation [35, 36].

$$C_0 = \frac{\pi \cdot \varepsilon_0 \cdot h_l}{\ln\left(h_l/a\right) - 1}, \tag{1}$$

where a is the radius of the rectangle and h is the half-length.

L_0 is chosen to resonate with C_0 at W_{02} and L_1 is chosen to resonate with C_1 at W_{02} [35, 36].

$$L_0 = \frac{1}{W_{02}^2 \cdot C_0}. \tag{2}$$

Table 1: Dipole antenna design parameters.

W_m	W_t	W_n	W_d	W_l
140	12.90	1	66	65
L_m	L_t	L_d	L_c	W_r
36.6	2.7	14.87	18.95	1.8

The estimated values of C_1, R_1, and L_1 are determined at the resonant frequency W_{01}, where the antenna reactance vanishes and the resistance equals R_0 [35, 36].

$$C_1 = \frac{A}{R_0^2 + A^2}\left(\frac{W_{01}}{W_{01}^2 - W_{02}^2}\right), \tag{3}$$

$$L_1 = \frac{R_0^2 + A^2}{A}\left(\frac{W_{01}}{W_{02}^2} - \frac{1}{W_{01}}\right), \tag{4}$$

$$R_1 = \frac{R_0^2 + A^2}{R_0}, \tag{5}$$

$$A = W_{01}L_0 - \frac{1}{W_{01}C_0}, \tag{6}$$

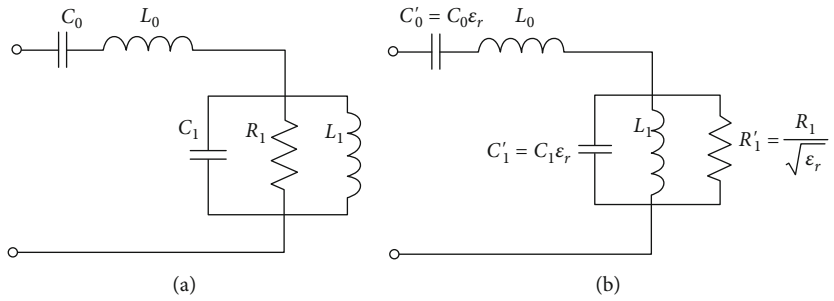

Figure 2: Dipole antenna equivalent circuit [35] in (a) a free space and (b) a lossy medium.

$$W_{01} = \frac{\pi c}{2h_l}\left[806.1 - 0.03043\left(\frac{h_l}{a}\right) + 1.060\times10^{-5}\left(\frac{h_l}{a}\right)^2 - 2.09\times10^{-9}\left(\frac{h_l}{a}\right)^3 + 51.59\ln\left(\frac{h_l}{a}\right) - 8.186\left(\ln\left(\frac{h_l}{a}\right)\right)^2 + 0.5502\left(\ln\left(\frac{h_l}{a}\right)\right)^3\right]\times10^{-3}, \quad (7)$$

$$W_{02} = \frac{\pi c}{2.h_l}\left[1108 + 0.1039\left(\frac{h_l}{a}\right) - 1.808\times10^{-5}\left(\frac{h_l}{a}\right)^2 + 2.203\times10^{-9}\left(\frac{h_l}{a}\right)^3 - 215.5\ln\left(\frac{h_l}{a}\right) + 51.59\left(\ln\left(\frac{h_l}{a}\right)\right)^2 - 3.85\left(\ln\left(\frac{h_l}{a}\right)\right)^3\right]\times10^{-3}. \quad (8)$$

As can be seen in Figure 2(b), if the antenna is located in a lossless medium characterized by the dielectric constant $\varepsilon = \varepsilon_0 \cdot \varepsilon_r$ and the permeability $\mu = \mu_0$, L_0 and L_1 remain unchanged and R_1 becomes $R_1' = R_1/\sqrt{\varepsilon_r}$. C_0 is transformed into $C_0' = C_0 \cdot \varepsilon_r$, where ε_0 is the dielectric constant in free space and ε_r is the relative dielectric constant of the medium, while C_1 is changed to $C_1' = C_1 \cdot \varepsilon_r$. Table 2 shows the comparative study between the theoretical analysis and the simulated analysis for the dipole antenna.

The antenna layout was simulated with Computer Simulation Technology (CST) Microwave Studio and modelled and optimized with Advanced Design System Environment (ADS). With the optimized parameters shown in Figure 3, a good agreement of the S_{11} results between the simulated antenna layout and the equivalent circuit diagram of the antenna modelled at 1 GHz can be achieved.

3. Split-Ring Resonator Configuration

This section presents a study of the split-ring resonator (SRR) with its equivalent circuit diagram. This resonator consists of a metal loop with a square shape and a gap on one side (Figure 4) [37]. As shown in Figure 4(c), the split-ring resonator is a type of RLC series resonant circuit. It consists of capacitive, inductive, and resistive load components,

Table 2: Comparative study between the analyzed element values within and without the lossless medium and the simulated parameter values for the dipole antenna.

Element values in a free space	Element values in a lossy medium	Parameter values
$C_0 = 0.46$ pF	$C_0' = C_0 \cdot \varepsilon_r = 1.15$ pF	$h = \frac{\lambda}{4} = \frac{c}{4f} = 0.065$ m
$L_0 = 13.7$ nH	$L_0 = 13.7$ nH	$a = \frac{\sqrt{b^2 + d^2}}{2} = 0.00063$ m
$R_1 = 196\,\Omega$	$R_1' = \frac{R_1}{\sqrt{\varepsilon_r}} = 124\,\Omega$	—
$L_1 = 12.02$ nH	$L_1 = 12.02$ nH	—
$C_1 = 0.25$ pF	$C_1' = C_1 \cdot \varepsilon_r = 0.4$ pF	—
—	$f_{res} = \frac{1}{2\pi\sqrt{L_0 C_0}} \simeq 1$ GHz	$f_{res} = \frac{C}{2.l} \simeq 1$ GHz

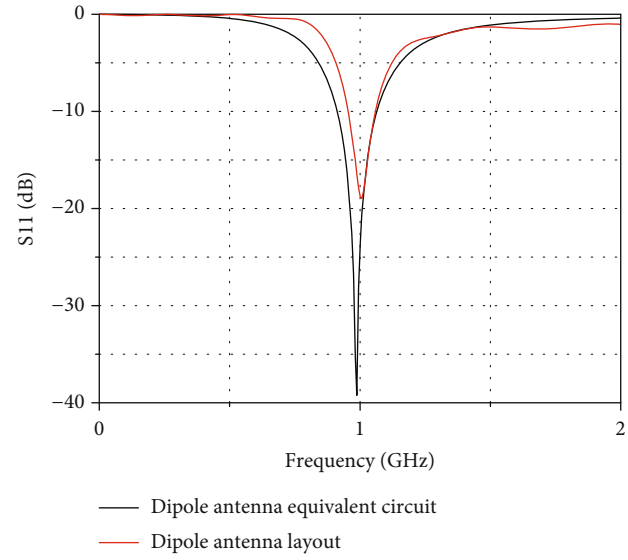

Figure 3: Simulated S_{11} of the equivalent circuit and layout of the dipole antenna.

which are symbolized by L, C, and R, respectively. The equivalent circuit diagram of the split-ring resonator structure can be represented by two LC series resonant circuits

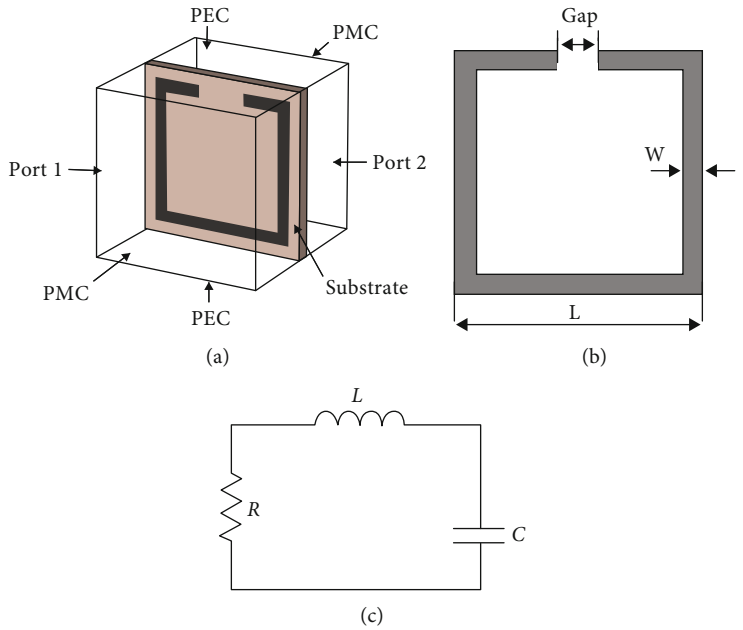

FIGURE 4: split-ring resonator unit cell: (a) boundary settings; (b) top side (c) equivalent circuit.

connected in parallel. By adjusting the ring length and the gap between the rings, the split-ring resonator configuration allows precise control of the resonant frequency at which the wave couples into the ring and forms a standing wave, resulting in a high electric field inside the gap. This precise control of the resonant frequency is particularly useful to achieve narrow banding given the small electrical size of the split-ring resonator relative to the wavelength. Therefore, the resonant frequency of split-ring resonator essentially depends on the inductance L, which is determined in particular by the shape and size of the ring, the capacitance C, and the resistance of the ring R.

Not only the resonant frequency but also the Q-factor of the resonant circuit can vary. The Q-factor is a measure of how sharply the split-ring resonator can distinguish between frequencies. A higher Q-factor indicates lower dissipative losses and better frequency selectivity. The Q-factor shows its dependence on the inductance L, capacitance C, and resistance R. This resistance represents the dissipative losses. It is a way of accounting for the energy that is dissipated as heat in the resonator and can directly influence on the (Q -factor) of the resonator. The Q-factor is higher when the resistance in the split-ring resonator equivalent circuit is low, which means that the resonator stores and releases energy more efficiently at its resonant frequency. Contrary, a higher resistance resulting in a lower Q-factor and higher losses leads to an effect on the performance of the split-ring resonator in applications such as antennas.

Figure 4(b) shows the design of the single split-ring resonator (SRR) unit cell. The split-ring resonator is placed on an Arlon CuClad 250LX substrate [38] with a dielectric constant of $\varepsilon_r = 2.42$ and a thickness of 0.49 mm. The dimensions of the split-ring resonator are $L = 11.95$ mm, gap = 3.3 mm, and $W = 0.55$ mm. In order to derive the reflection and transmission coefficients of the split-ring resonator, two wave ports are made in the left and right areas of the box as can be seen in Figure 4(a). The curve of the reflection coefficient for the split-ring resonator cell is shown in Figure 5(a). The metamaterial has a transmission coefficient (S_{12}) of -45 dB and -48 dB when operating at a frequency of 2.5 GHz and 5.8 GHz, respectively. Figure 5(b) shows the real part of the effective permeability curve for a split-ring resonator. Based on equation (9) [31], it is obvious that the permeability in the frequency range of 2.41-2.8 GHz has negative values exactly at the resonance point at 2.5 GHz. Similarly, this resonator has a second negative μ_{eff} value around the resonant frequency 5.3 to 7 GHz. The presence of negative values for permeability highlights the particular behavior of the metamaterial and categorizes it as a left-handed medium (LHM). To better understand how the split-ring resonator works, Figure 6 shows the distributions of surface currents within the split-ring resonator structure. This plot is shown specifically for the frequency corresponding to the operation of the split-ring resonator. It can be seen that the double resonant frequency is due to the inductive and capacitive effect that occurs in the metallic conductive paths and gab, respectively.

$$\mu_{\text{eff}} = \pm\sqrt{\frac{(1+S_{11})^2 - S_{12}^2}{(1-S_{11})^2 - S_{12}^2}}. \tag{9}$$

Before proceeding to the next section, let us discuss the reason for choosing the split-ring resonator in our proposed antenna design. The split-ring resonator offers advantages such as the following:

(i) -Easy and precise control over the two specific RFID frequencies (2.45 GHz and 5.8 GHz)

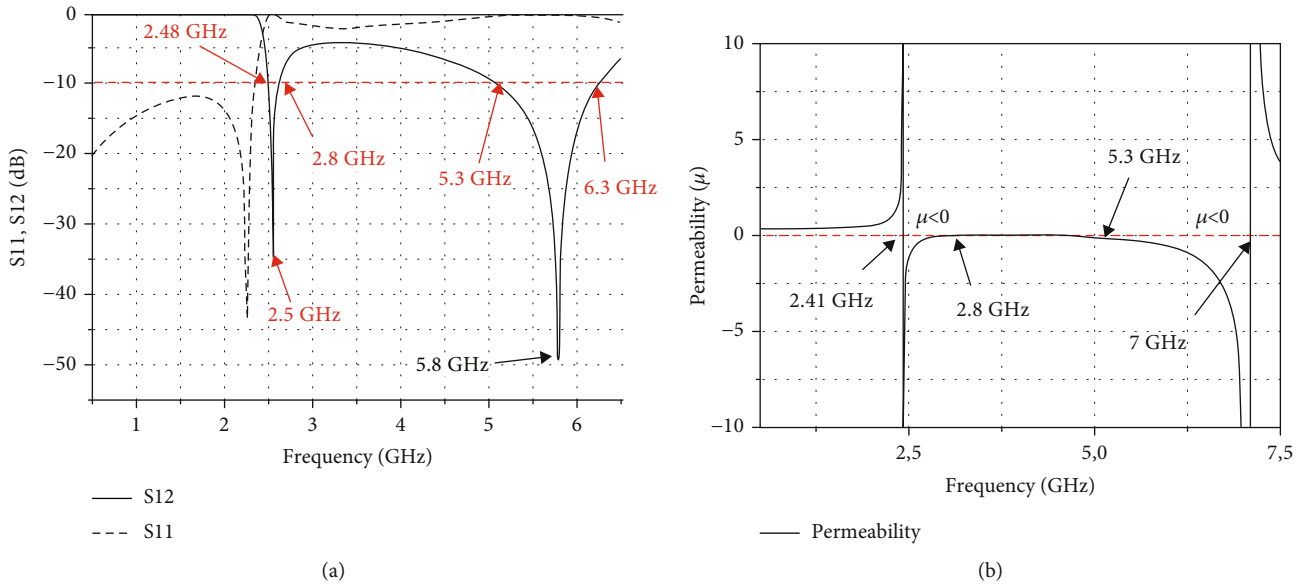

FIGURE 5: (a) Simulated S_{11} and S_{12} and (b) permeability of the split-ring resonator structure.

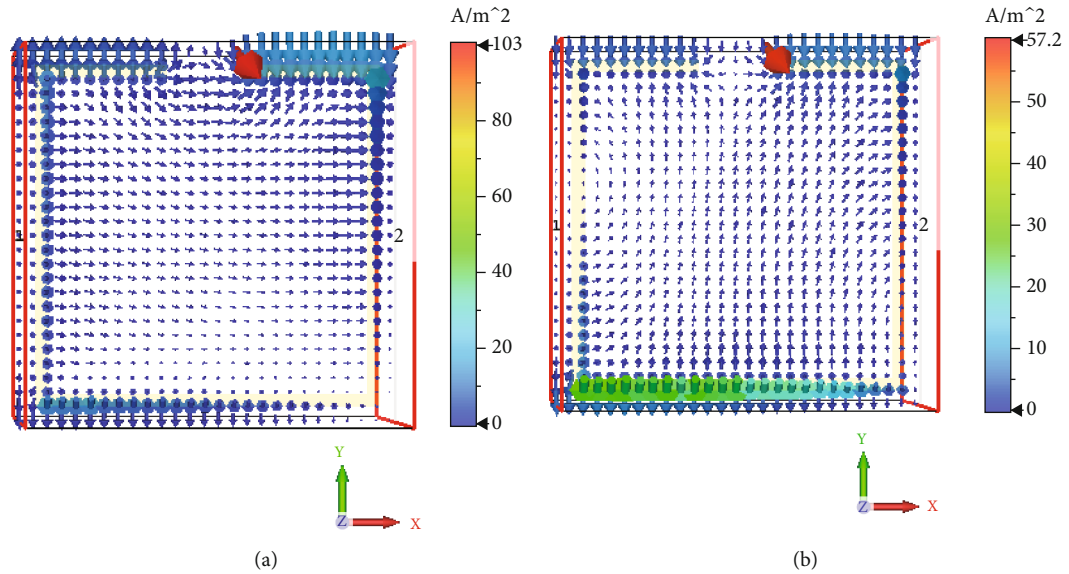

FIGURE 6: Simulated surface currents distributions of the split-ring resonator at (a) 2.5 GHz and (b) 5.8 GHz.

(ii) -Split-ring resonator can generate negative effective permeability in the 2.45 GHz and 5.8 GHz operating frequencies, resulting in unique electromagnetic effects that can improve the radiation properties of the dipole antenna

(iii) Split-ring resonator can influence the impedance matching of the dipole antenna, as good impedance matching has been achieved in its dual band. Thus, efficient power transfer between the dipole antenna and the split-ring resonator can maximize the power radiated by the proposed metamaterial antenna

Finally, we can assert that the decision to utilize split-ring resonator over other resonators is based on its tailored suitability for achieving multiband antenna with high gain that aligns with our specific goals.

4. Antenna Design Methodology Using Metamaterials

In this section, the performance characteristics of a dipole antenna with an integrated split-ring resonator array are investigated in different orientations: 0°, 90°, 180°, and 270° (see Figure 7). The split-ring resonator array is positioned around the radiating element on the top and bottom of the Arlon CuClad 250LX substrate (see Figure 8) to investigate the effects of its orientation on the radiation characteristics of the dipole antenna, such as impedance matching and

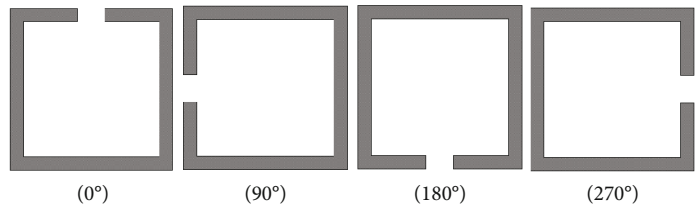

Figure 7: Various orientations of the split-ring resonator.

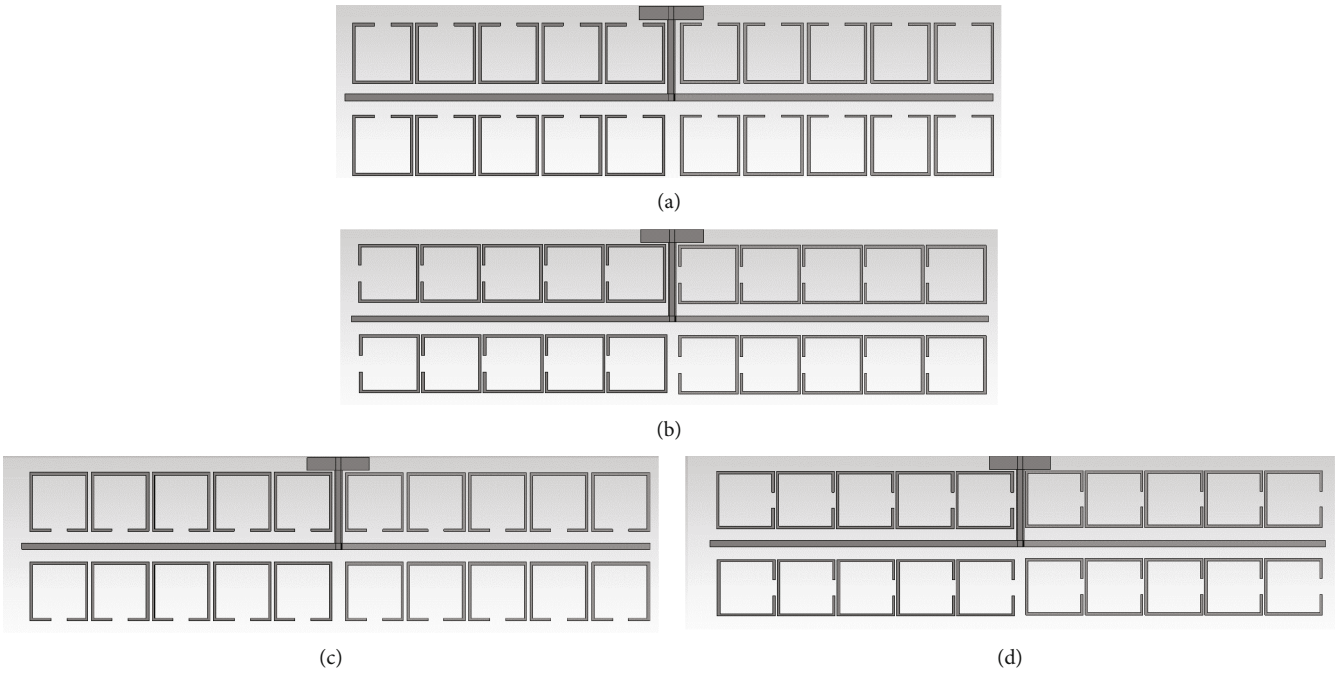

Figure 8: Dipole antenna with an array of (a) 0° SRR, (b) 90° SRR, (c) 180° SRR, and (d) 270° SRR.

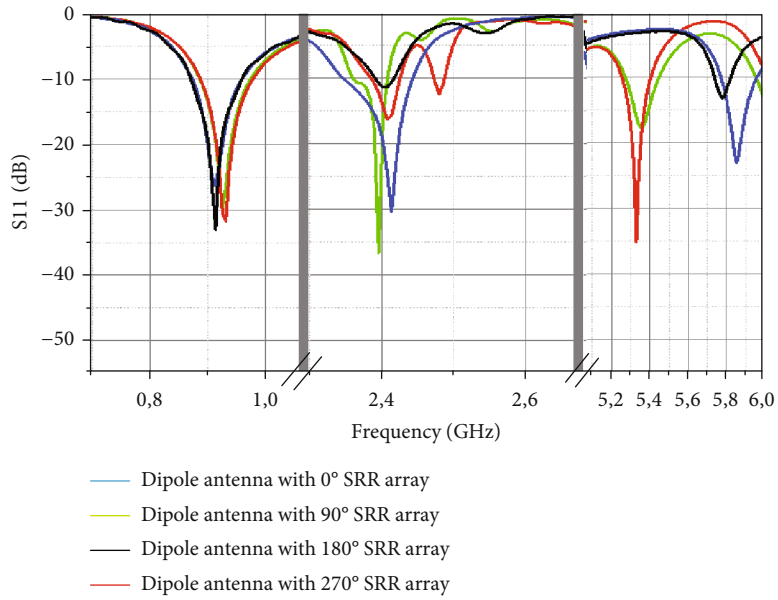

Figure 9: Simulated S_{11} of the dipole antenna with different orientations of the split-ring resonator.

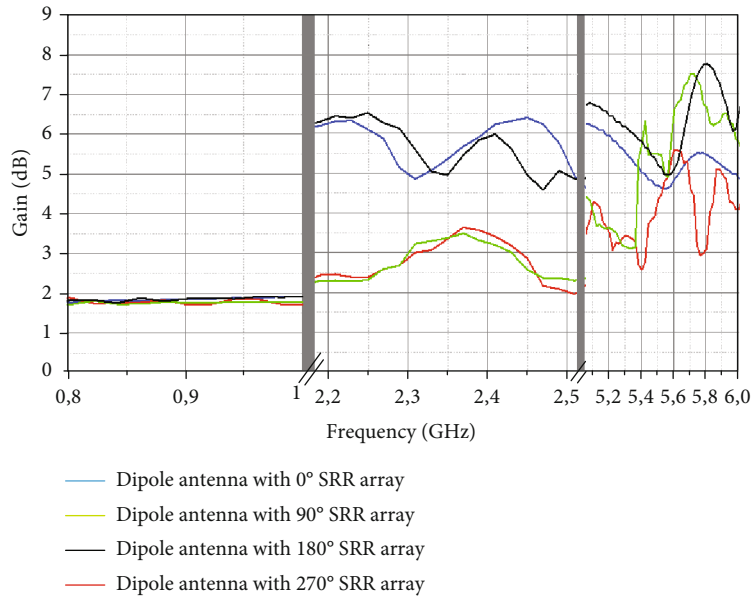

FIGURE 10: Simulated realized gain of the dipole antenna with different orientations of the split-ring resonator.

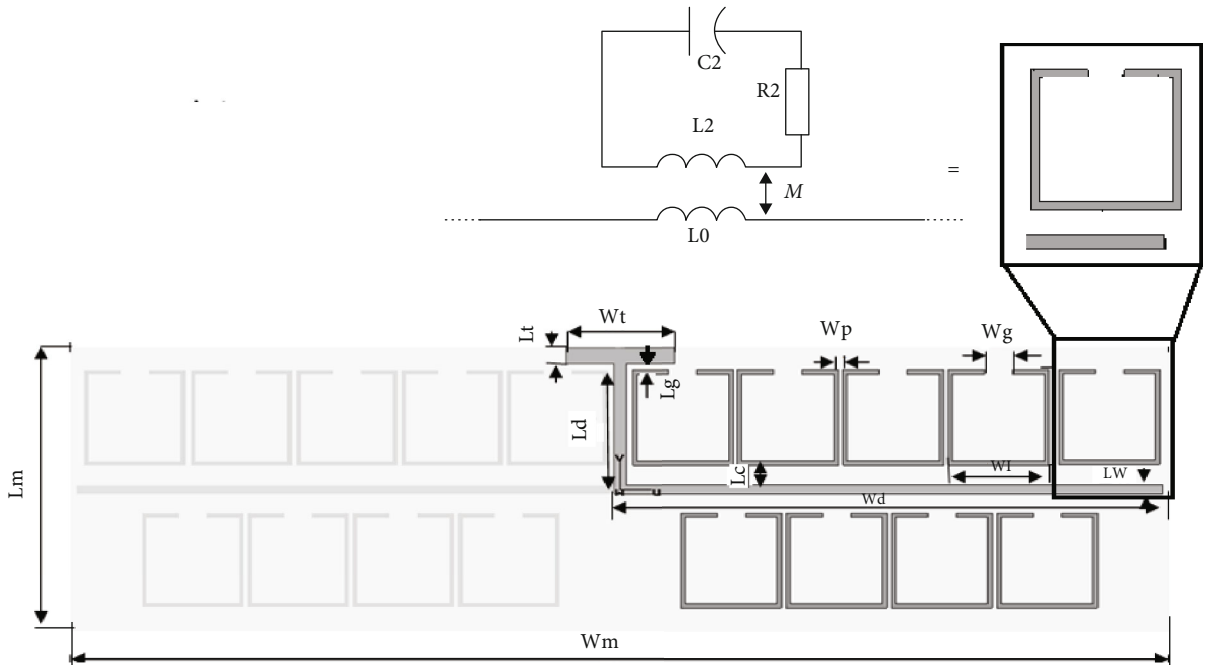

FIGURE 11: Geometry of the proposed dipole antenna with an alternating arrangement of split-ring resonator array at 0° orientation and its equivalent circuit analysis.

realized gain. The performance of the antennas is evaluated using the Microwave Studio (CST) software.

Figure 9 shows the *S*-parameter simulations used to investigate the effect of the different split-ring resonator orientations on the reflection coefficient of the antennas. It can be observed that the S_{11} curves in the UHF band show a high degree of consistency for all orientations, indicating similar antenna characteristics in this frequency range in all positions. The inclusion of a split-ring resonator array in the dipole antenna lowers the resonant frequency to 915 MHz

TABLE 3: Proposed metamaterial antenna design parameters.

W_m	L_c	L_g	L_w	W_t
140	2.48	0.25	1.34	12.90
L_m	W_p	W_l	L_d	L_t
36.6	0.75	11.95	14.80	2.7

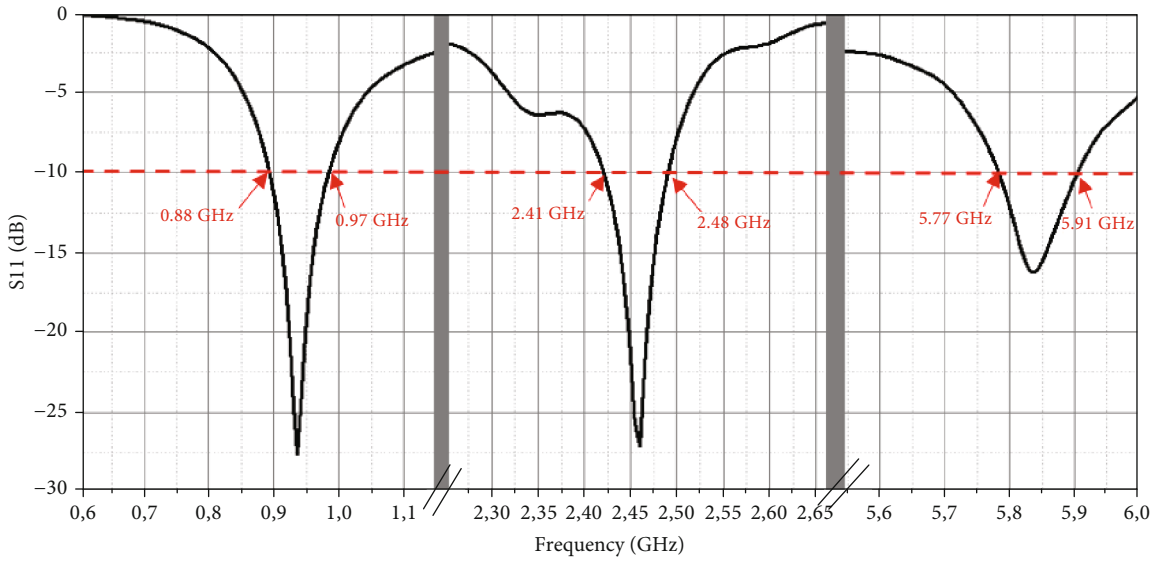

FIGURE 12: Simulated S_{11} of the proposed dipole antenna with an alternating arrangement of split-ring resonator array at 0° orientations.

compared to Figure 3 and at the same time generates another resonant frequency at 2.4 GHz, which corresponds to the resonant frequency of the split-ring resonator (see Figure 5(a)). This could be due to a stronger electromagnetic interaction between the antenna and the split-ring resonator array. Conversely, in the SHF band, there is a clear divergence in the S_{11} curve for a dipole antenna with a 0° split-ring resonator array. This divergence indicates a stronger influence on the operation of the antenna in the SHF frequency band when the split-ring resonator array is positioned at an angle of 0°. The corresponding resonant frequencies for the dipole antenna with a 0° split-ring resonator array are as follows: 0.88-0.97 GHz, 2.37-2.46 GHz, and 5.77-5.87 GHz. The gap of the split-ring resonator changes the effective capacitance, which in turn changes the resonant frequencies. Consequently, the orientation of the gap in a (SRR) has a significant influence on the reflection coefficient of the antenna features.

Figure 10 shows the curve of the achieved gain for the dipole antenna with different split-ring resonator orientations at 0°, 90°, 180°, and 270°. Within the frequency band of 0.8-1 GHz, the realized gain remains almost the same for all antennas, with each having an estimated realized gain of 1.9 dB. At 2.4 GHz, a significant increase in realized gain to 6.5 dB is observed for dipole antennas with 0° and 180° split-ring resonator orientations, as compared to those with 90° and 270° split-ring resonator orientation, which means that split-ring resonator orientation at 0° and 180° has a greater impact on antenna performance at this specific frequency. In the entire SHF band, the achieved gain varies between 4 dB and 6.6 dB. The dipole antennas with 0° and 180° split-ring resonator show a slight improvement compared to the antennas with 90° and 270° SSR in the same frequency band. This observation indicates that 0° and 180° split-ring resonator orientations lead to better antenna performance in the UHF and SHF bands. Furthermore, the result shows that the symmetry of the split-ring resonator on the antenna has no influence on the overall performance. Therefore, certain split-ring resonator orientations could possibly contribute to improved antenna performance.

To simplify the analysis, we focus on specific antennas with split-ring resonator array orientations at 0°, since the SRR orientation at 0° is similar to that at 180°. The innovative technique integrates the split-ring resonator array into the dipole antenna with an alternating arrangement, as shown in Figure 11. This arrangement method intentionally changes the interaction between the dipole antenna and the split-ring resonator array. Consequently, this modification can lead to changes in the electromagnetic coupling results and impedance matching characteristics. All design parameters are listed in Table 3.

Figure 12 shows the curve of the reflection coefficient for a dipole antenna with an alternating split-ring resonator array at 0°. It can be observed that the antenna with a 0° split-ring resonator array has peaks in certain frequency bands. These include 0.88-0.97 GHz, 2.41-2.48 GHz, and 5.77-5.91 GHz. It is noticeable that these frequencies correspond well with the frequencies of the three-band RFID applications (860-960 MHz and 2.4 GHz/5.8 GHz). As can be seen in Figure 12, the proposed antenna also shows excellent impedance matching at the resonant frequencies.

Figure 13 shows the curve of the realized gain of the proposed metamaterial antenna. Compared with Figure 10, the alternating arrangement of 0° split-ring resonator arrays shows a higher realized gain, reaching 7 dB at the frequency of 2.47 GHz, which is consistent with the RFID frequency range, albeit with a slight upward shift. As can be seen in Figure 13, the antenna gain curve increases in the third range, showing a peak of 6 dB in the RFID frequency range from 5.725 GHz to 5.850 GHz and reaches a maximum of 7 dB at 5.91 GHz, with the maximum gain outside the frequency band of 5.8 GHz with a slight upward shift, representing a significant increase in performance. This is understandable as in a 0° configuration, the split-ring

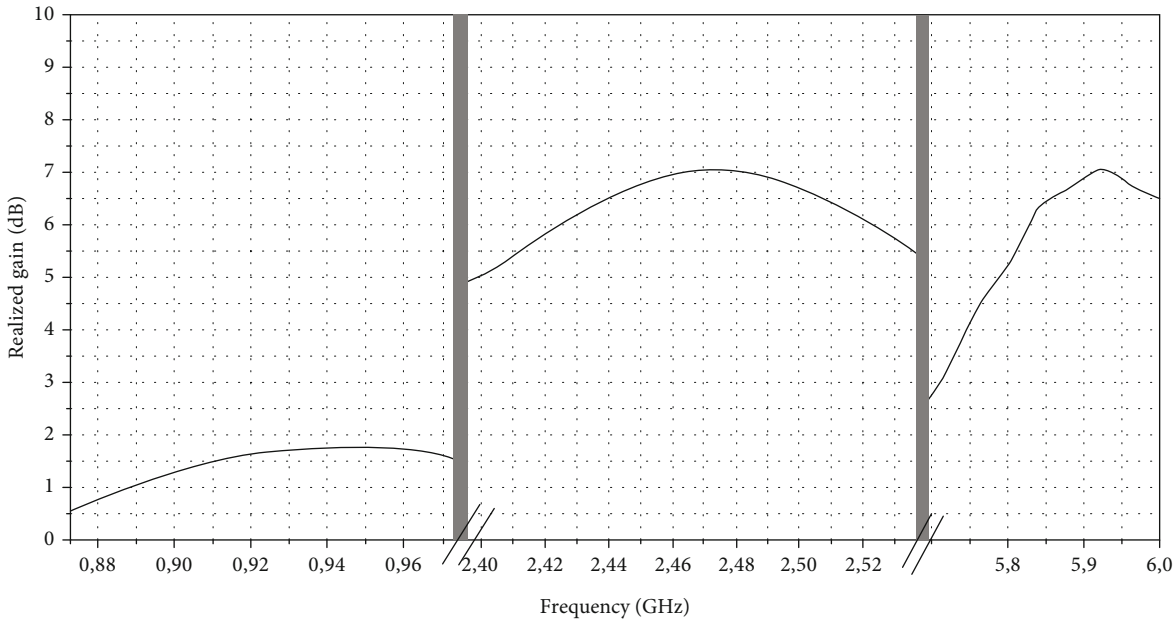

Figure 13: Simulated realized gain of the proposed dipole antenna with an alternating arrangement of split-ring resonator array at 0° orientations.

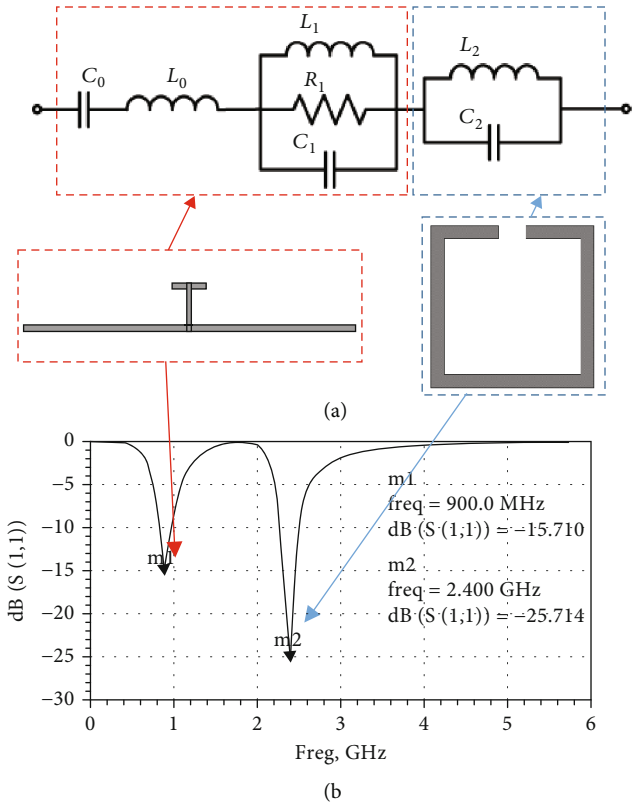

Figure 14: SRR-loaded antenna: (a) equivalent circuit [36]; (b) simulated S_{11} using ADS.

Table 4: Element values of equivalent circuit for metamaterial dipole antenna.

Elements	Geometry
$C_0{}'$	1.15 pF
L_0	13.7 nH
$R_1{}'$	50 Ω
L_1	12.02 nH
$C_1{}'$	0.4 pF
C_2	1.1 pF
L_2	6.9 nH

resonator array runs parallel to the antenna elements, which can influence the direction of wave propagation and amplify the signal strength in a particular direction. To summarize, the alignment of the split-ring resonator array at 0° with an alternating array integrated into the dipole antenna can significantly affect the performance of the antenna. Similar to the split-ring resonator equivalent circuit, the metamaterial antenna can also be simplified to a simple parallel *LC* tank circuit [39]. However, to design an antenna based on SRRs, equivalent circuit models are required. SRRs can be excited both magnetically and electrically [40]. However, it has been confirmed that magnetic coupling is the dominant mechanism in SRRs. The proposed equivalent circuit model for the loaded split-ring resonator antenna is shown in Figure 14. L_0 is the inductance of the dipole antenna, while the split-ring resonator is modelled as resonant tank circuits (with inductance L_2 and capacitance C_2) that are magnetically connected to the dipole antenna via a mutual

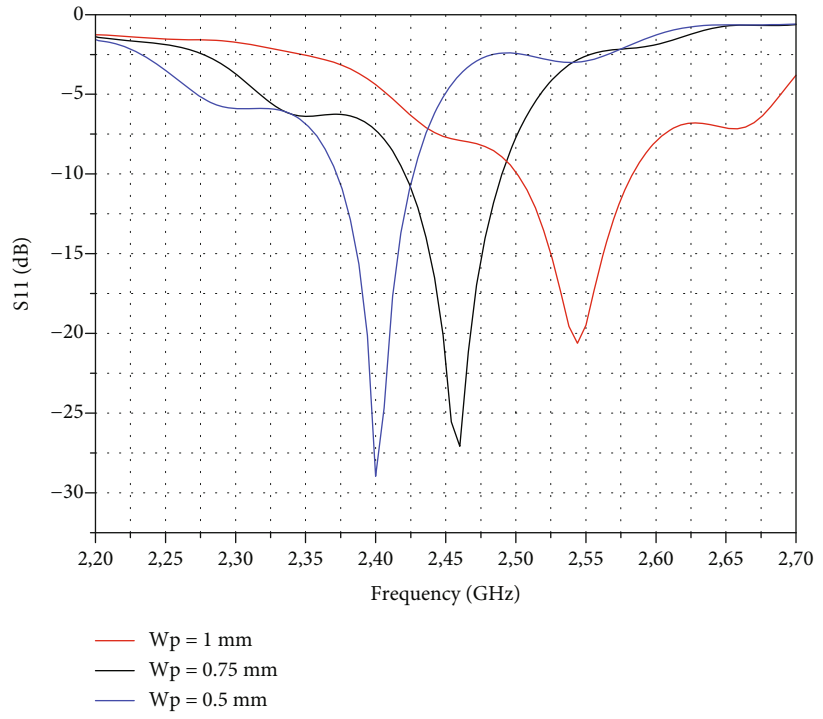

(a)

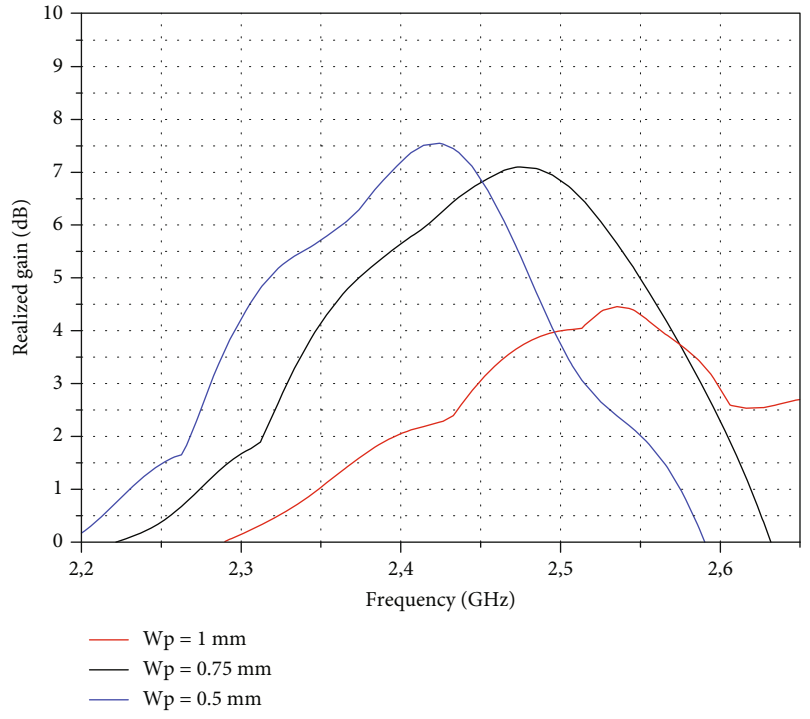

(b)

FIGURE 15: The effect of parameter W_p on (a) simulated S_{11} and (b) simulated realized gain.

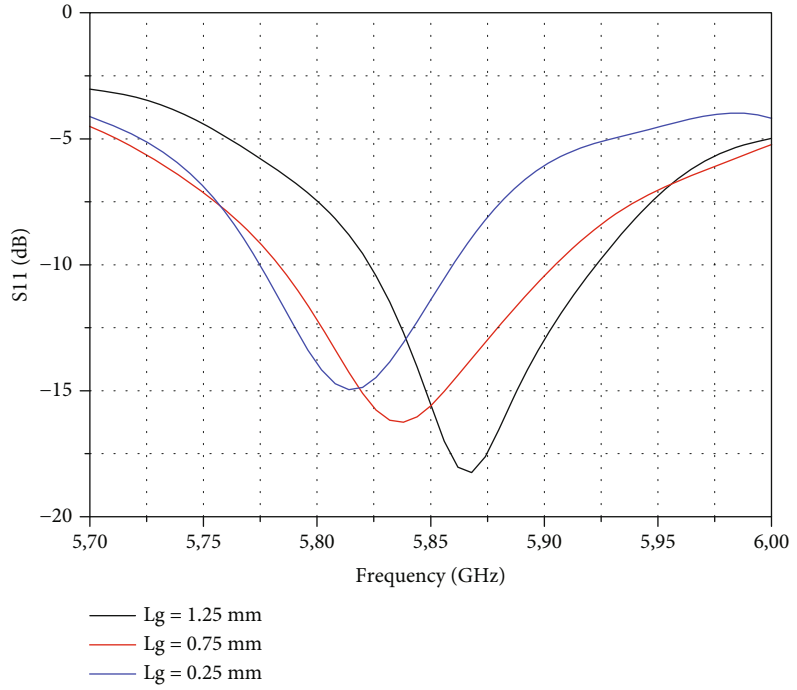

(a)

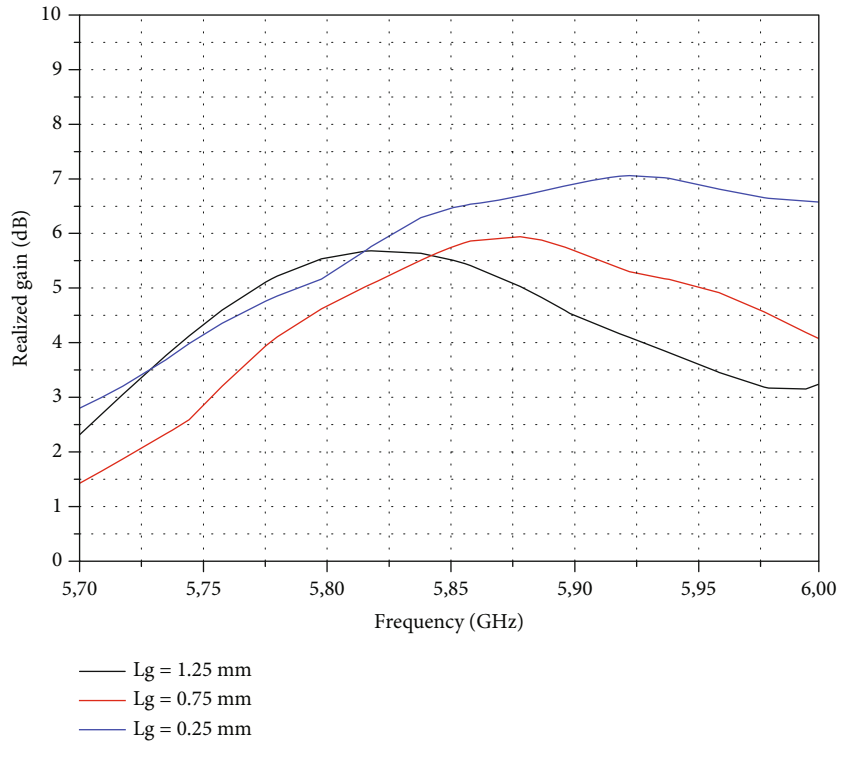

(b)

FIGURE 16: The effect of parameter L_g on (a) simulated S_{11} and (b) simulated realized gain.

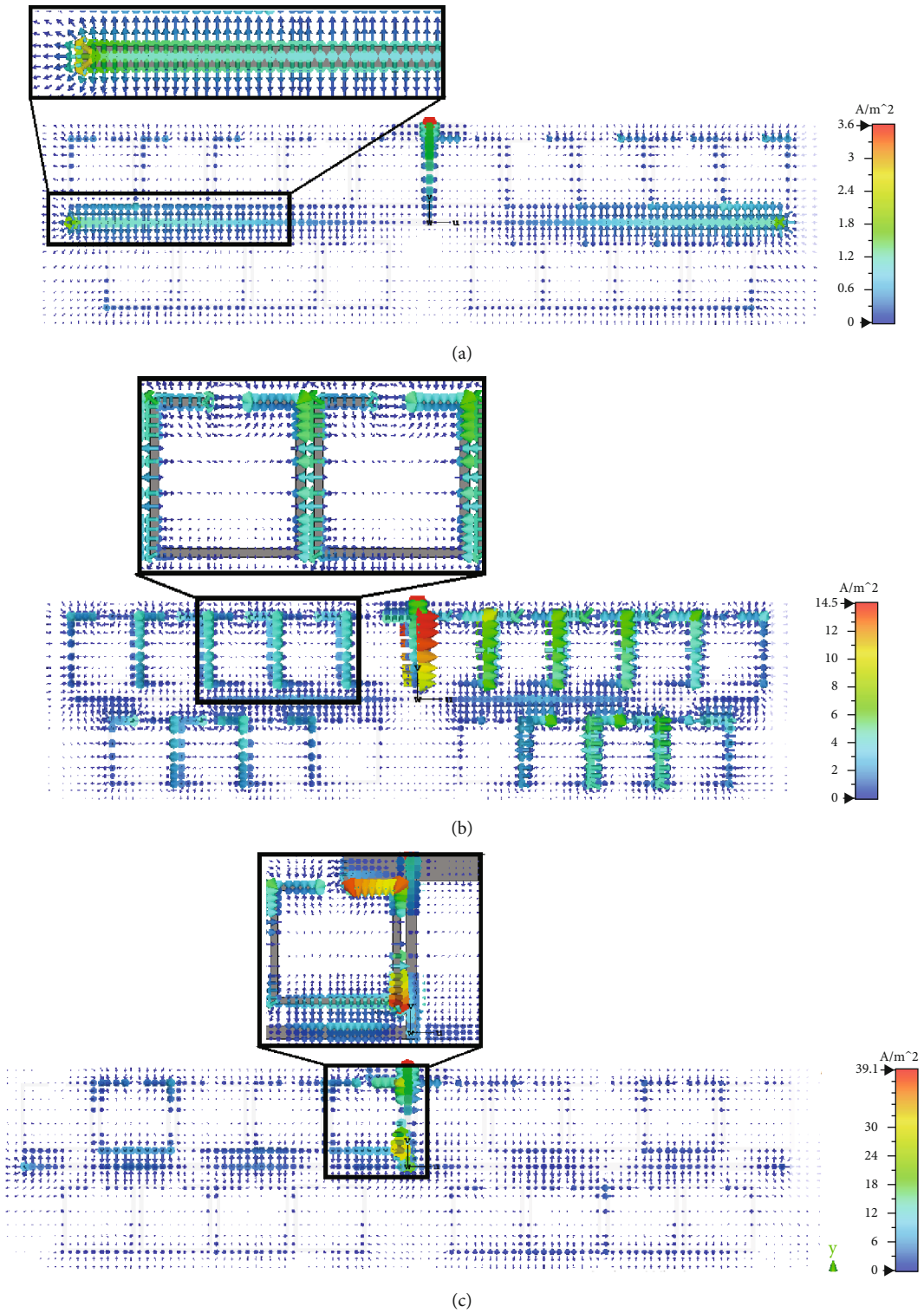

Figure 17: Surface current distribution on the proposed metamaterials dipole antenna at (a) 0.915 GHz, (b) 2.45 GHz, and (c) 5.8 GHz.

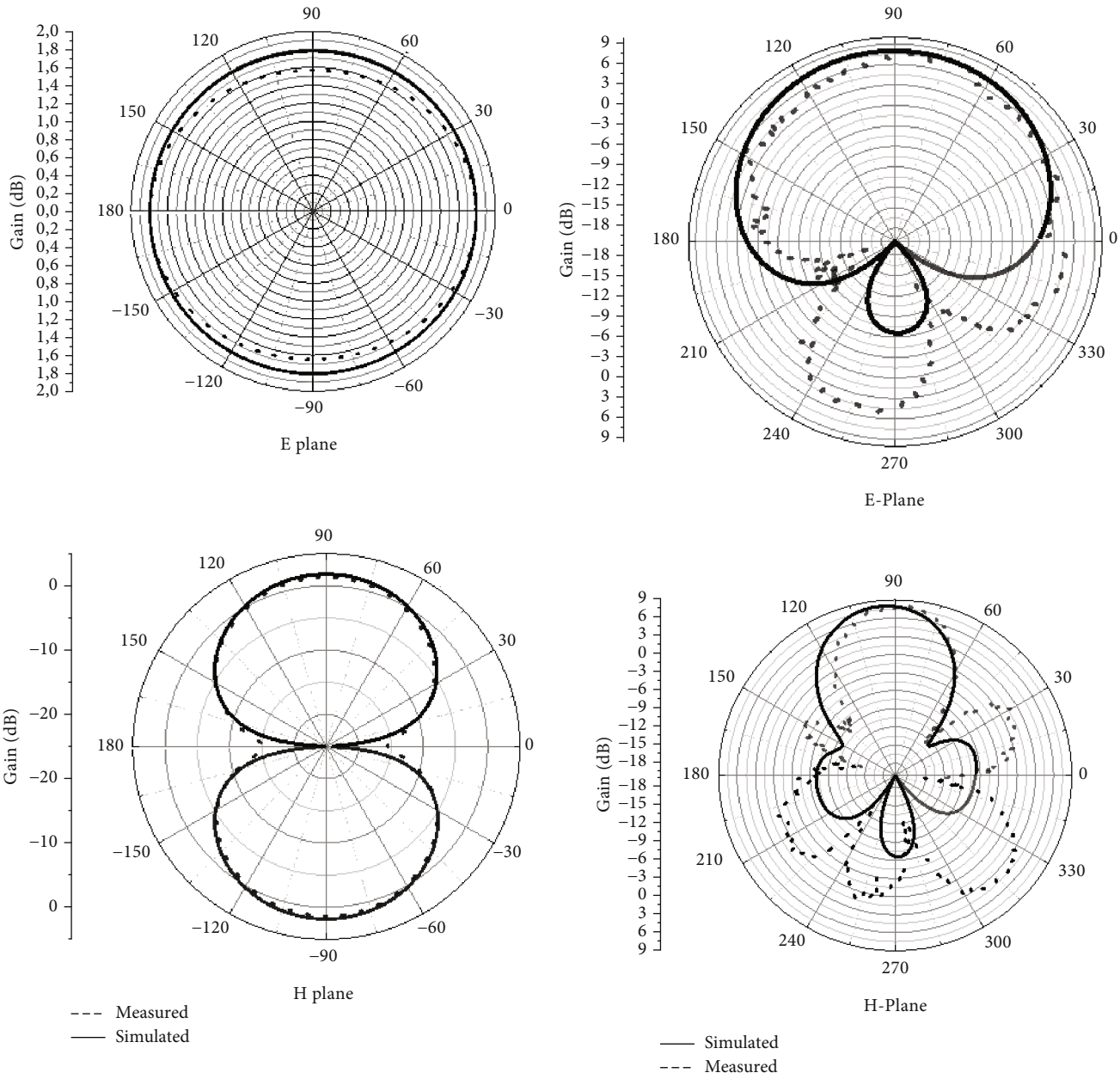

Figure 18: Continued.

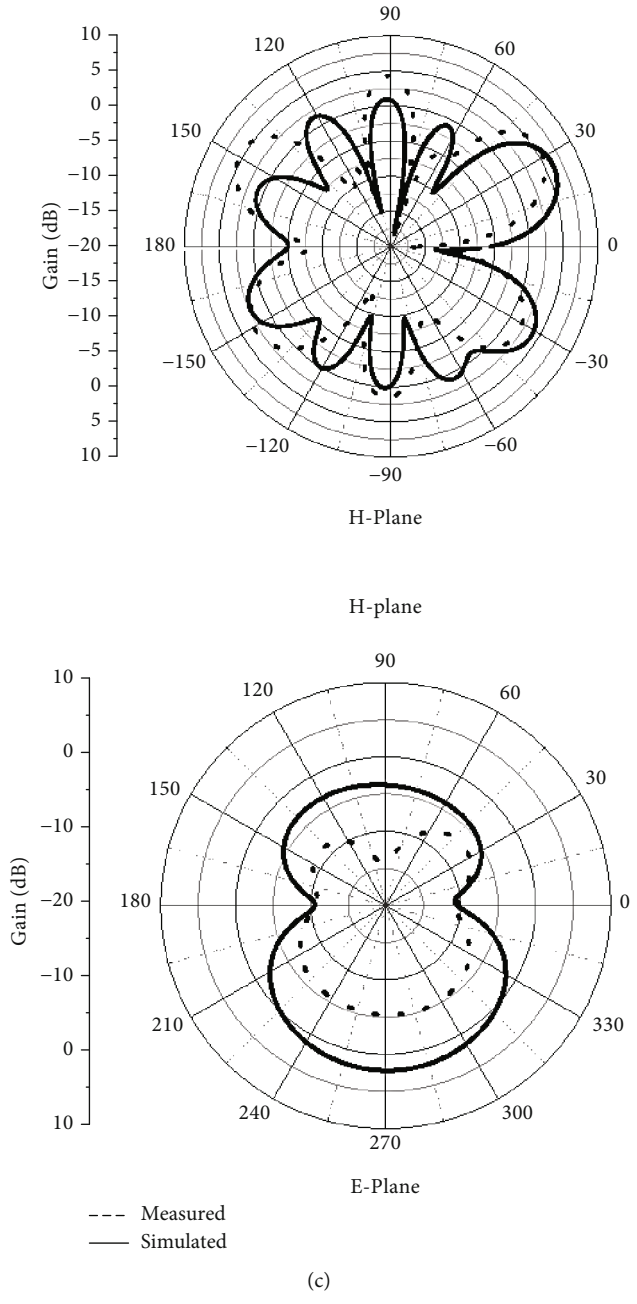

(c)

Figure 18: Simulated and measured radiation patterns of the proposed metamaterial dipole antenna at different frequencies, (a) 0.915 GHz, (b) 2.45 GHz, and (c) 5.8 GHz, in E and H planes.

inductance M. The values of inductance L_2 and capacitance C_2 can be obtained using the following equations [35, 36].

$$L_2 = \frac{hL_{\text{unit}}}{F}, \tag{10}$$

$$C_2 = \frac{2 \cdot h \cdot \mu_{\text{eff}}}{L_{\text{unit}} \pi^2 c^2}, \tag{11}$$

where μ_{eff} is the relative permeability and h is the half-length. L_{unit} and L_{fp} represent the additional inductance per unit length which can be calculated using the following equations [35, 36]:

$$L_{\text{unit}} = \frac{\mu_0}{2\pi}\left[\mu_r - \frac{1}{\varepsilon_r}\right] \ln\left(\frac{a}{b}\right), \qquad L_{\text{fp}} = L_{\text{unit}} \cdot h, \tag{12}$$

where ε_r is the relative permittivity, μ_r is the relative permeability, and μ_0 is the permeability in free space. F is an unknown factor that can be expressed as follows [35, 36]:

$$F = 1 + \frac{1}{1 - (2 \cdot K_{\text{eff}} \cdot h)^2/\pi^2} \cdot \left(\frac{\sin^2(K_{\text{eff}} \cdot h)}{1 - \sin 2k_{\text{eff}} \cdot h/2 \cdot K_{\text{eff}} \cdot h - 1} \right), \tag{13}$$

where the wave number K_{eff} can be approximated by $K_{\text{eff}} = (w/c)\sqrt{\varepsilon_{\text{eff}}\mu_{\text{eff}}}$, ε_{eff} is the effective relative permittivity, w is the angular frequency, and K_0 is the free space wave number.

Considering (3)–(5), (10), and (11), the estimated values of circuit elements can be obtained and are indicated in Table 4.

5. Parametric Study and Optimization of the Proposed Antenna

Investigation through a parametric study is crucial to understand the impact of each parameter on antenna characteristics, paving the way for antenna effectiveness optimization. In this analysis, only a single parameter is adjusted while the others remain stable. By integrating a split-ring resonator array with a dipole antenna, an interesting physical phenomenon occurs, namely, W_p, the spacing between the SRRs. This value plays a decisive role in determining the frequency at 2.47 GHz. This can be seen in Figure 15(a). A lower W_p value leads to a higher capacitive effect, making the antenna more efficient at lower frequencies, while a higher W_p value increases the resonant frequency, making the antenna suitable for higher frequencies. Furthermore, the influence of W_p is not limited to frequency. It can also influence other important communicative properties such as the gain of the antenna. Changing the physical structure of the split-ring resonator array can change the radiation pattern and possibly transform the typical dipole antenna into a more directional structure, which improves the gain of the antenna up to 7.6 dB, as a smaller spacing between the rings generally leads to a higher gain (see Figure 15(b)). The realized gain can reach 8.3 dB with a further decrease in this parameter.

In addition, L_g, which is the mutual capacitance between the ground plane and the split-ring resonator, can significantly influence the characteristics of the antenna. The value of L_g can control the resonant frequency of the proposed metamaterial antenna at 5.8 GHz, as shown in Figure 16(a). When the value of L_g is increased, the mutual capacitance decreases, which increases the resonant frequency due to the lower storage of electric field energy and leads to a higher resonant frequency. Conversely, if L_g is reduced, the electrical length of the antenna increases, and the resonant frequency decreases, as the electric field increases due to the greater charge storage between the ground plane and the split-ring resonator array. Figure 16(a) therefore shows a direct relationship between L_g and the resonant frequency of the proposed antenna. L_g changes can also indirectly affect the radiation pattern and gain of the antenna by changing the current distribution. As can be seen in Figure 16(b), by adjusting the parameter L_g, we can manipulate the realized gain of the antenna for specific applications, which underlines its central role in improving the performance of the antenna as needed.

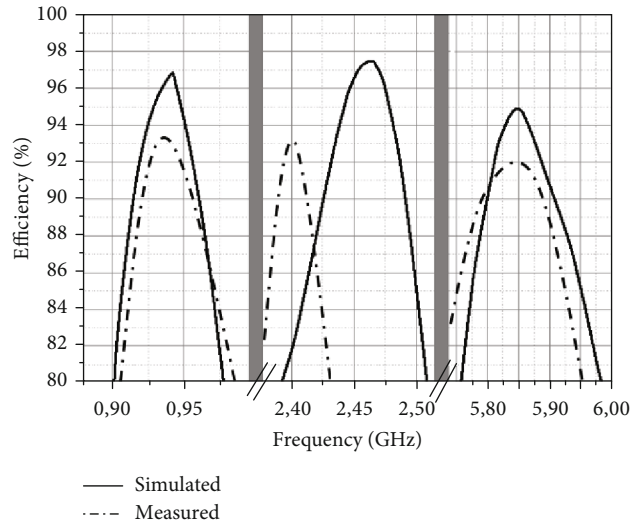

Figure 19: Simulated and measured efficiencies of the dipole antenna with an alternating arrangement of split-ring resonator array at 0°.

6. Results and Discussion

6.1. Simulated Surface Current Analysis. The distribution of the surface current in a dipole antenna with an alternating arrangement of split-ring resonator arrays at 0° orientation over different frequencies is shown in Figure 17. From Figure 17(a), it can be seen that the current mainly flows in the arms of the dipole antenna at 0.915 GHz, indicating that these parts mainly act as radiating elements. This frequency is close to the resonant frequency of the antenna without metamaterials. At 2.4 GHz (Figure 17(b)), the current peaks at the entire edge of the split-ring resonator array, suggesting that this frequency coincides with the resonant frequency of the split-ring resonator. At 5.8 GHz (Figure 17(c)), the current is mainly distributed between the split-ring resonator and the ground plane, indicating that this coupling leads to a response at this frequency. In addition, the current mainly circulates around the alternating split-ring resonator array, suggesting that their arrangement is affecting the behavior of the antenna.

6.2. Radiation Pattern and Efficiency. The radiation patterns of the measurement and the simulation are shown both in the E plane and in the H plane at the individual resonance modes 0.915, 2.45, and 5.8 GHz (see Figure 18). A high degree of agreement is observed between the simulated and measured results. Furthermore, due to the symmetrical dipole structure, the antenna shows an omnidirectional radiation pattern in both planes above 0.915 GHz, as shown in Figure 18(a). At the frequency of 2.45 GHz, the result shows that the proposed antenna in combination with metamaterials has a directional radiation pattern in the E plane and H plane. As can be seen in Figure 18(b), the interaction of

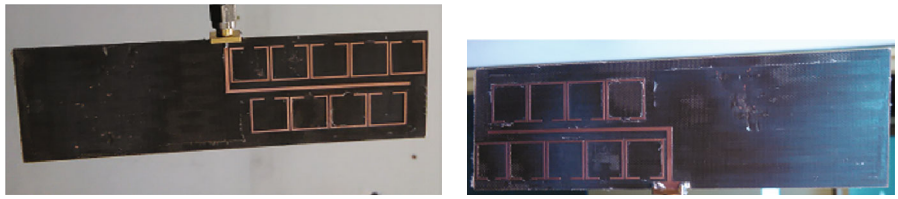

(a) (b)

Figure 20: Photograph of the proposed metamaterials antenna: (a) top side; (b) bottom side.

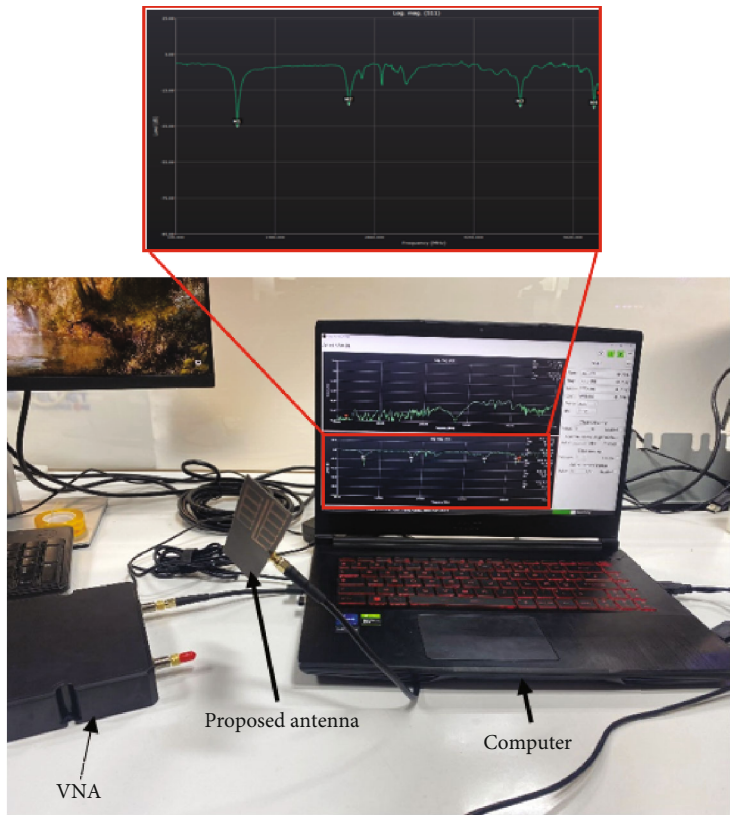

Figure 21: Setup to measure S_{11} parameter of the proposed antenna.

the electromagnetic field is affected by the redistributed split-ring resonator array at an angle of 0°, which changes the current distribution on the antenna element and increases the performance of the antenna in terms of gain. The split-ring resonator arrays improve the antenna's ability to focus the radiated energy in selected directions by effectively storing electrical energy in their structures and changing the field distribution around the antenna. As can be seen in Figure 18(b), the gain of the metamaterial antenna increases to 7 dB and it exhibits a more directional pattern. Figure 18(c) shows a clear deterioration of the radiation pattern at 5.8 GHz. This degradation can be attributed to the wider bandwidth exhibited by the split-ring resonator at this frequency. In other words, when the split-ring resonator has a narrow bandwidth (see the first SRR resonant frequency in Figure 5(a)), the antenna shows a more specific response to the resonant frequency, which affects the directional radiation pattern in this range (this can be interpreted in

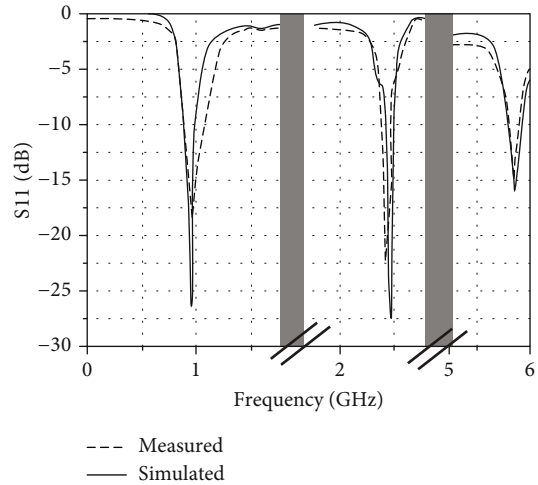

Figure 22: Simulated and measured S_{11} of the proposed metamaterials antenna.

Table 5: Comparison of the proposed antenna with other recent multiband antennas for similar applications.

Year of pub	Ref	Antenna dimensions (mm^3)	Electrical size (λ_0^3)	Operating bands (GHz)	Realized gain (dB)	Eff (%)	Applications	Techniques
2019	[3]	$100 \times 160 \times 1.6$	—	920-925/2.45	4.37		RFID	Slots
2020	[5]	$112 \times 100 \times 1.6$	—	1.3/2.6	1.85/1.89	—	—	Slots
2021	[7]	103×38	—	0.8/2.4/2.8/6.2	1.4/2.16/ 2.54	—	IoT/Wi-Fi	Change the antenna shape
2021	[10]	$12 \times 46 \times 0.5$	$0.375 \times 0.098 \times 0.004$	2.45/5.5	2.28/4.42	97/98	WLAN	Change the antenna shape
2022	[11]	$86 \times 86 \times 1.6$	$0.25 \times 0.25 \times 0.04$	0.915/2.45/5.8	2/5.1/5.7		RFID	Multilayer
2020	[14]	$70 \times 63 \times 6$	—	2.4/5.95	5/4.7	—	RFID/5G/sub-6GHz/WLAN	Multilayer
2020	[16]	$104 \times 72.5 \times 1.6$	—	915/2.45	5	—	RFID	Stacked patches
2023	[17]	$16 \times 130 \times 0.5$	—	2.34–2.56/ 5.07–5.90	3.89/4.88 5.79/7.18	87 73	WLAN	Stacked patches
2020	[26]	$30 \times 30 \times 0.8$	$0.3 \times 0.3 \times 0.008$	2.65–3.25/5–7	2.18/3.25	97/99	WLAN	MTM
—	This work	$131.6 \times 34 \times 0.49$	$0.39 \times 0.11 \times 0.0014$	0.915/2.45/5.8	1.8/7/7	97/98//95	Triband RFID	MTM

Figure 18(b)). In contrast, a wider bandwidth (see the second SRR resonant frequency in Figure 5(a)) allows for more flexible operation over a range of frequencies. In summary, the resonator allows the antenna to operate over a wider frequency range with greater flexibility, which in turn affects the radiation pattern at 5.8 GHz.

The simulated and measured efficiencies of the metamaterial antenna are shown in Figure 19. The antenna shows peak overall efficiencies of 97%, 98%, and 95%, respectively, in the three operating bands. The proposed antenna offers stable efficiencies throughout. However, the efficiency decreases in the nonresonant band. Figure 19 shows a small discrepancy between the measured efficiency and the simulated efficiency curve. This can be attributed to several factors, such as the minimum spacing ($W_p = 0.5$ mm and $L_g = 0.25$ mm), which may have caused problems during fabrication or measurement, as the values of L_g and W_p play a crucial role in controlling the performance of the proposed antenna, as shown in Figures 15(b) and 16(b), and consequently may have a negative impact on the measured efficiency, or the placement of the antenna during the measurement setup.

6.3. Fabrication and Measurement. To validate the numerical analysis, a prototype is fabricated (see Figure 20) and tested (see Figure 21) according to the final optimization to achieve the perfect antenna design. Figure 22 shows the simulated and measured S_{11} of the proposed metamaterial antenna. Following the results, there is a great agreement between the simulated and tested results for S_{11}, although there was a small shift in the tested results. This phenomenon could be due to several aspects, including the manufacturing discrepancy and the influence of the SMA connector.

7. State-of-the-Art Comparison

Table 5 contains a detailed comparison of the proposed antenna with other recent multiband antennas for similar applications. When evaluating the performance, it is noticeable that the gain of the microstrip antennas in the UHF band is at most 6 dB [11–16]. Unfortunately, this is not an excellent result, as it can lead to losses in network coverage, especially for RFID, which limits their practical application. The antenna presented in this paper has a higher gain in certain frequency bands, especially in the UHF band, reaching up to 7 dB, which emphasizes the superiority of our design in this aspect. Moreover, the antennas in references [10, 14, 26] operate on two bands and have miniaturized size but are inadequate compared to our proposed design. This comparison shows that our antenna can cover more bands than the other designs. Importantly, the proposed antenna utilizes a simple geometry with a single probe feed, eliminating the need for a complex structure and multilayer substrate as called for in references [11, 14]. This design promotes low weight, low profile, and low fabrication cost due to the planar structure, which is a clear advantage of the proposed antenna. Comparing our design with the existing literature, it is clear that our proposed antenna outperforms the existing designs and establishes itself as a strong contender for RFID applications that require a high gain multiband antenna.

8. Conclusion

In this study, a high gain multiband antenna was analyzed and investigated by a novel approach of integrating a symmetrical split-ring resonator array with alternating array at 0° orientation into a dipole antenna. The results of the work have shown that the proposed antenna design provides a

clear discrimination between all operating bands in terms of good impedance matching and excellent efficiency. In addition, an in-depth parametric analysis was performed to understand the physics behind the antenna's performance enhancement without the need for augmentation or additional circuitry. The metamaterial antenna has several advantages, such as lighter weight and easy fabrication due to its simple design, and it can cover the triple band of RFID applications.

Data Availability

The data used in this study are included in the figures.

Conflicts of Interest

The authors declare that they have no conflicts of interest.

References

[1] A. El Yassini, S. Ibnyaich, S. Chabaa, and A. Zeroual, "Miniaturized broadband multiband planar antenna with a symmetric quarter circular ground plane for WLAN/WiMAX standards," *Microwave and Optical Technology Letters*, vol. 62, no. 9, pp. 2953–2964, 2020.

[2] J. Cui, A. Zhang, and S. Yan, "A novel compact dual-band circular/linear polarization switchable slot annular antenna with filtering network," *International Journal of RF and Microwave Computer-Aided Engineering*, vol. 31, no. 9, article e22767, 2021.

[3] A. Romputtal and C. Phongcharoenpanich, "IoT-linked integrated NFC and dual band UHF/2.45 GHz RFID reader antenna scheme," *IEEE Access*, vol. 7, pp. 177832–177843, 2019.

[4] V. K. Pandit and A. R. Harish, "A compact CPW-fed tapered monopole triple-band antenna for WLAN/WiMAX application," *Microwave and Optical Technology Letters*, vol. 60, no. 9, pp. 2298–2303, 2018.

[5] R.'e. Malallah, R. M. Shaaban, and A. Wa'il, "A dual band star-shaped fractal slot antenna: design and measurement," *AEU-International Journal of Electronics and Communications*, vol. 127, article 153473, 2020.

[6] P. M. Mpele, F. M. Mbango, D. B. O. Konditi, and F. Ndagijimana, "A tri-band and miniaturized planar antenna based on countersink and defected ground structure techniques," *International Journal of RF and Microwave Computer-Aided Engineering*, vol. 31, no. 5, article e22617, 2021.

[7] D. Singh, K. R. Jha, and S. K. Sharma, "Nearly omni-directional compressed multiband flexible and conformal dipole antenna," *International Journal of RF and Microwave Computer-Aided Engineering*, vol. 31, no. 8, article e22732, 2021.

[8] A. De, B. Roy, and A. K. Bhattacharjee, "Miniaturized dual band consumer transceiver antenna for 5G-enabled IoT-based home applications," *International Journal of Communication Systems*, vol. 34, no. 11, article e4840, 2021.

[9] K. Kumari, R. K. Jaiswal, and K. V. Srivastava, "A compact triple band circularly polarized planar antenna for wireless application," *Microwave and Optical Technology Letters*, vol. 62, no. 7, pp. 2611–2617, 2020.

[10] K. Zhang and S. Yan, "Compact omnidirectionaldual-banddipole antenna with reduced ground plane effect," *Microwave and Optical Technology Letters*, vol. 63, no. 6, pp. 1753–1759, 2021.

[11] E. Zhang, A. Michel, P. Nepa, and J. Qiu, "Multifeed tri-band circularly polarized antenna for UHF/MW-RFID application," *International Journal of RF and Microwave Computer-Aided Engineering*, vol. 32, no. 1, Article ID e22939, 2022.

[12] J. Liang, G.-. L. Huang, S. Zhang, T. Yuan, G.-. M. Zhang, and M. Amin, "Compact differential-fed dual-band antenna via loading shorting pin," *International Journal of RF and Microwave Computer-Aided Engineering*, vol. 28, no. 9, article e21497, 2018.

[13] P. Mathur and G. Kumar, "Dual-band dual-polarized microstrip antenna at S-and X-bands using feed technique for suppression of interference due to higher order modes," *International Journal of RF and Microwave Computer-Aided Engineering*, vol. 31, no. 11, article e22870, 2021.

[14] S.-. J. Li, W.-. J. Lu, and L. Zhu, "Dual-band stacked patch antenna with wide e-plane beam width and stable gain at both bands," *Microwave and Optical Technology Letters*, vol. 63, no. 4, pp. 1264–1270, 2021.

[15] A. M. Jie, N. Nasimuddin, M. F. Karim, and K. T. Chandrasekaran, "A dual-band efficient circularly polarized rectenna for RF energy harvesting systems," *International Journal of RF and Microwave Computer-Aided Engineering*, vol. 29, no. 1, article e21665, 2019.

[16] S. Fu, A. Xiong, W. Chen, and S. Fang, "A compact planar Moxon-Yagi composite antenna with end-fire radiation for dual-band applications," *Microwave and Optical Technology Letters*, vol. 62, no. 6, pp. 2328–2334, 2020.

[17] K.-J. Lee, K. Lee, and T.-H. Lee, "Printed collinear dipole array antenna with a horizontally omnidirectional pattern for dual-band WLAN," *Microwave and Optical Technology Letters*, vol. 65, no. 2, pp. 671–678, 2023.

[18] O. P. Falade, M. Ur-Rehman, X. Yang, G. A. Safdar, C. G. Parini, and X. Chen, "Design of a compact multiband circularly polarized antenna for global navigation satellite systems and 5G/B5G applications," *International Journal of RF and Microwave Computer-Aided Engineering*, vol. 30, no. 6, article e22182, 2020.

[19] S. Koziel and A. Bekasiewicz, "Rapid redesign of multiband antennas with respect to operating conditions and material parameters of substrate," *International Journal of Numerical Modelling: Electronic Networks, Devices and Fields*, vol. 33, no. 6, article e2723, 2020.

[20] M. El Atrash, M. A. Abdalla, and H. M. Elhennawy, "A wearable dual-band low profile high gain low SAR antenna AMC-backed for WBAN applications," *IEEE Transactions on Antennas and Propagation*, vol. 67, no. 10, pp. 6378–6388, 2019.

[21] S. Nallapaneni and P. Muthusamy, "Design of multiband fractal antenna loaded with parasitic elements for gain enhancement," *International Journal of RF and Microwave Computer-Aided Engineering*, vol. 31, no. 6, article e22622, 2021.

[22] Y. Xu, Z. Zhang, A. Wang, and J. Hou, "Design of three multi-branch microstrip antennas compatible with WiMAX/WiFi/4G/5G NR for coal mine applications," *Microwave and Optical Technology Letters*, vol. 65, no. 3, pp. 892–900, 2023.

[23] M. Shaw, N. Mandal, and M. Gangopadhyay, "A compact circularly polarized isosceles triangular microstrip patch antenna with parasitic elements for multiband application," *Microwave and Optical Technology Letters*, vol. 62, no. 10, pp. 3275–3282, 2020.

[24] E. M. Malathy, V. Thanikachalam, and N. Manikandan, "Metamaterial-loaded multiband antenna for embedded automotive Internet-of-Things communications," *International Journal of Communication Systems*, vol. 34, no. 15, article e4941, 2021.

[25] R. K. Saraswat and M. Kumar, "A metamaterial hepta-band antenna for wireless applications with specific absorption rate reduction," *International Journal of RF and Microwave Computer-Aided Engineering*, vol. 29, no. 10, article e21824, 2019.

[26] M. A. Abdalla, M. El Atrash, N. A. El-Sobky, and S. R. Zahran, "Concept and analysis of a coupled split-ring resonator for wide-/dual bands, self-filtering, high out-of-band suppression and highly efficient antennas," *International Journal of Microwave and Wireless Technologies*, vol. 13, no. 2, pp. 126–136, 2021.

[27] R. Sahoo and D. Vakula, "Compact metamaterial inspired conformal dual-band antenna loaded with meander lines and fractal shaped inductor for Wi-Fi and WiMAX applications," *IET Microwaves, Antennas & Propagation*, vol. 13, no. 13, pp. 2349–2359, 2019.

[28] E. Yassini, L. A. Abdessalam, S. Ibnyaich, S. Chabaa, and A. Zeroual, "Design of circular patch antenna with a high gain by using a novel artificial planar dual-layer metamaterial superstrate," *International Journal of RF and Microwave Computer-Aided Engineering*, vol. 29, no. 11, article e21939, 2019.

[29] Z. Zaalouni, S. Beldi, and A. Gharsallah, "Study of miniaturized E-patch antenna loaded with novel E-shape SRR metamaterial for RFID applications," *International Journal of RF and Microwave Computer-Aided Engineering*, vol. 29, no. 6, article e21698, 2019.

[30] M. Abdelkarim, S. Naoui, L. Latrach, and A. Gharsallah, "Improvement of the frequency characteristics for RFID patch antenna based on C-shaped split-ring resonator," *International Journal of Advanced Computer Science and Applications*, vol. 9, no. 2, 2018.

[31] M. Abdelkarim, S. Naoui, L. Latrach, and A. Gharsallah, "Performance improvement of RFID reader antenna using spiral split-ring resonators," *International Journal on Communications Antenna and Propagation*, vol. 6, no. 6, 2016.

[32] A. P. Dhande and K. C. B. Rao, "Significance of split-ring resonator to design multiband operation by coupling with monopole," *International Journal of Applied Engineering Research*, vol. 13, no. 1, pp. 647–650, 2018.

[33] F. J. Herraiz-Martínez, L. Enrique García-Muñoz, D. González-Ovejero, V. González-Posadas, and D. Segovia-Vargas, "Dual-frequency printed dipole loaded with split-ring resonators," *IEEE Antennas and wireless propagation letters*, vol. 8, pp. 137–140, 2009.

[34] S. Dakhli, J. M. Floch, K. Mahdjoubi, H. Rmili, and H. Zangar, "Compact and multi-band metamaterial-inspired dipole antenna," in *In 2013 7th European Conference on Antennas and Propagation (EuCAP)*, pp. 2765–2768, Gothenburg, Sweden, 2013.

[35] Y. Liao, T. H. Hubing, and D. Su, "Equivalent circuit for dipole antennas in a lossy medium," *Ieee Transactions On Antennas And Propagation*, vol. 60, no. 8, pp. 3950–3953, 2012.

[36] Y. Liao, T. H. Hubing, and S. Donglin, "Equivalent circuit with frequency-independent lumped elements for coated wire antennas," *IEEE Transactions on Antennas and Propagation*, vol. 60, no. 11, pp. 5419–5423, 2012.

[37] K. J. Dehning, M. Hitzemann, A. Gossmann, and S. Zimmermann, "Split-ring resonator based sensor for the detection of amino acids in liquids," *Sensors*, vol. 23, no. 2, p. 645, 2023.

[38] M. Abdelkarim, S. Naoui, L. Latrach, and A. Gharsallah, "Design of a compact size tag antenna based on split-ring resonator for UHF RFID application," *Intnational Journal of RF and Microwave Computer-Aided Engineering*, vol. 29, no. 7, article e21607, 2018.

[39] L. Smith, V. Shiran, W. Gomaa, and T. Darcie, "Characterization of a split-ring-resonator-loaded transmission line at terahertz frequencies," *Optics Express*, vol. 29, no. 15, 2021.

[40] R. Marques, F. Martin, and M. Sorolla, *Metamaterials with negative parameters theory, design, and microwave applications*, John Wiley & Sons, 1st edition, 2008.